 doi:10.20944/preprints202207.0048.v1

Article

A Contrast Minimization Approach to Quantify and Remove Sun Glint in Landsat 8 / OLI Imagery

Frank Fell

Informus GmbH, 13187 Berlin, Germany; fell@informus.de

Abstract: Sun glint, i.e., direct solar radiation reflected from a water surface, negatively affects the accuracy of ocean color retrieval schemes if entering the field-of-view of the observing instrument. Herein, a simple and robust method to quantify the sun glint contribution to top-of-atmosphere (TOA) reflectances in the visible (VIS) and near-infrared (NIR) is proposed, exploiting concomitant observations of the sun glint's morphology in the shortwave infrared (SWIR) characterized by reflectance contrasts typically higher than those resulting from other in-water or atmospheric processes. The proposed method, termed Glint Removal through Contrast Minimization (GRCM), requires high spatial resolution (ca. 10–50 m) imagery to resolve the sun glint's characteristic morphology, meeting additional criteria on radiometric resolution and temporal delay between the individual band's acquisitions. It has been applied with good success to a selection of Landsat 8 (L8) Operational Land Imager (OLI) scenes encompassing a wide range of environmental conditions in terms of observation geometry and glint intensity, as well as aerosol and Rayleigh optical depth. The method proposed herein is entirely image based and does not require ancillary information on the sea surface roughness or related parameters (e.g., surface wind), neither the presence of clear water areas in the image under consideration. Limitations of the proposed method are discussed, and its potential for sensors other than OLI as well as applications beyond glint removal is sketched.

Keywords: ocean color; sun glint; atmospheric correction; Landsat 8

1. Introduction

In Earth Observation (EO), the term "glint" refers to specular reflection of direct (sun glint) or diffuse (sky glint) solar radiation. Sun glint frequently poses a problem in remote observations of aquatic ecosystems as it may outshine the water leaving radiance carrying the signal of interest over large areas, thereby "confusing" water constituent retrieval schemes.

The intensity of sun glint is controlled by the presence of sea surface facets allowing reflection of direct solar radiation into the field-of-view of the observing instrument. Nadir looking imagers are therefore predominantly affected by sun glint at rather small solar zenith angles, while wide-swath instruments may also be affected by sun glint at larger solar zenith angles. Illustrating the importance of the problem, a number of ocean observing instruments on polar orbiting platforms have been equipped with mechanisms to reduce the exposure to sun glint, as for example the currently operational Ocean, Land and Cloud Imager (OLCI) instruments onboard the Sentinel 3 series of satellites, tilted 12.6° westwards [1].

Significant efforts have been made over the last decades to establish procedures to remove sun glint from ocean color observations. A thorough review of the approaches available by 2009 is provided in [2]. Information on sun glint correction methods published thereafter can be found for example in [3] and [4].

Earlier attempts to estimate and remove the sun glint contribution from medium resolution (ca. 300–1000 m) ocean color imagery combined statistical models of the sea surface facet orientation with radiative transfer calculations [5]. Such methods depend critically on the availability of concomitant external information, for example on the wind

Preprints (www.preprints.org) | NOT PEER-REVIEWED | Posted: 4 July 2022 doi:10.20944/preprints202207.0048.v1

field controlling the orientation of the sea surface facets [6]. This information is not always available at the required accuracy, geographic detail, and temporal resolution which is why these methods have not consistently provided the anticipated results in operational applications.

A different approach has been adopted by [7] and [8] for high resolution (≤ 10 m) multispectral imagery by establishing image and channel specific linear relationships to estimate the sun glint contribution in the visible (VIS, ca. 0.4 - 0.7 μm) from concomitant observations in the near infrared (NIR, ca. 0.7 - 1.5 μm), assuming negligible sub-surface contribution at the latter wavelengths. The linear coefficients are obtained by statistical regression applied to clear water areas encompassing both glint and glint-free pixels. A similar approach has been applied by [9], who developed a simple empirical model for medium resolution (250 – 1000 m) MODIS-AQUA imagery to be applied over the Gulf of Mexico exploiting information in the NIR at 0.859 μm to estimate the sun glint contribution in the VIS at 0.469 μm, 0.555 μm, and 0.645 μm. [10] have applied the regression approach to four years of OLI 8 imagery offshore French Guiana, making use of the SWIR OLI channel B7 (2.2 μm) to estimate the glint contribution.

A different approach has been implemented by [11], who use a pixel-based spectral matching technique (POLYMER, POLYnomial based algorithm applied to MERIS) to disentangle the sun glint contribution from the atmospheric and the in-water contributions. POLYMER is based on an iterative optimization scheme relying on relatively simple models of the atmospheric and oceanic composition; the quality of the glint retrieval therefore depends on how well the underlying models represent reality.

The recent advent of a new generation of space-borne imagers providing observations in the shortwave infrared (SWIR, ca. 1.5 – 2.5 μm) at high spatial (ca. 30 m or higher) and radiometric (12 bit or better) resolution such as the Landsat 8 (L8) Operational Land Imager (OLI) has opened the path for the development of optimized sun glint correction schemes. Due to the strong absorption of pure water, the water leaving radiance at SWIR wavelengths can reasonably assumed to be zero [12], such that the TOA reflectance above water surfaces in the SWIR can be approximated as consisting of contributions from surface and atmosphere only. Taking advantage of the availability of SWIR observations, a sun glint correction method for the Multi-Spectral Imager (MSI) onboard the Sentinel-2 series of satellites has been developed by [4], using TOA observations to determine the bidirectional reflectance distribution function (BRDF) for a SWIR reference channel, and a theoretically derived model of the BRDF spectral dependency to subsequently assess the glint contribution at shorter wavelengths.

In the present article, a new method to estimate the sun glint contribution to the TOA reflectance in OLI images is introduced, combining elements of previously published approaches with a novel way of identifying and quantifying sun glint. While a linear model is applied to estimate the sun glint in the VIS and NIR (further on referred to as VNIR) from concomitant observations in the SWIR as suggested in [7] and [8], the model coefficients are estimated in the present work by exploiting the sun glint's characteristic morphology through a contrast minimization approach, hence the designation GRCM (Glint Removal through Contrast Minimization). The main advantage of this new approach as compared to the above-mentioned regression-based methods lies in the fact that no clear water areas need to be present in the area to be glint corrected.

2. Materials and Methods

2.1. Data sources and processing

2.1.1. The Operational Land Imager (OLI)

The Operational Land Imager (OLI) flown onboard Landsat 8 provides operational imagery since 18 March 2013. The satellite orbits the Earth in a sun-synchronous, near-polar orbit with an inclination of 98.2 degrees at an altitude of 705 km crossing the equator at a Mean Local Time (MLT) of 10:00 a.m. ± 15 minutes. OLI disposes of nine spectral bands ranging from the VIS to the SWIR at 12-bit radiometric resolution (**Table 1**).

Preprints (www.preprints.org) | NOT PEER-REVIEWED | Posted: 4 July 2022 doi:10.20944/preprints202207.0048.v1

Despite its name, and as evidenced by a large number of studies [13] (and references therein), OLI is well suited for the observation of aquatic ecosystems due to its significantly improved radiometric resolution and signal-to-noise ratio (SNR) as compared to its predecessors TM/ETM+ [14].

Table 1. Characteristics of the OLI spectral bands as specified in the Landsat 8 Data Users Handbook [15].

Spectral band	Spectral range	Spatial resolution	SNR
B1, Coastal / Aerosol	0.435-0.451 µm	30 m	238
B2, Blue	0.452-0.512 µm	30 m	364
B3, Green	0.533-0.590 µm	30 m	302
B4, Red	0.636-0.673 µm	30 m	227
B5, NIR	0.851-0.879 µm	30 m	204
B6, SWIR-1	1.566-1.651 µm	30 m	265
B7, SWIR-2	2.107-2.294 µm	30 m	334
B8, Pan	0.503-0.676 µm	15 m	149
B9, Cirrus	1.363-1.384 µm	30 m	165

2.1.2. OLI Level-1 to Level-2 conversion

Landsat 8 OLI Collection 2 Level 1 Terrain Precision (L1TP) data of Tier 1 have been used for the present work, offering consistent geo-registration within prescribed tolerances of <12 m radial root mean square error (RMSE) [16]. TOA reflectances have been calculated for each spectral band from the coefficients provided through the scene-specific metadata file according to the procedure described in Section 5.2 of [15]:

$$\rho^{TOA} = \left(M_\rho \times Q_{cal} + A_\rho\right) / \cos\left(\theta_{SOL}\right), \quad (1)$$

where ρ^{TOA} is the planetary reflectance at TOA [unitless], M_ρ is the reflectance multiplicative scaling factor, A_ρ is the reflectance additive scaling factor, Q_{cal} is the Level 1 pixel value in Digital Numbers (DN), and $cos\left(\theta_{SOL}\right)$ is the cosine of the local solar zenith angle.

For all investigated scenes, $M_\rho = 2.0 \times 10^{-5}$. The reflectance change per unit Q_{cal} therefore amounts to:

$$\Delta\rho^{TOA} \text{ per unit } Q_{cal} = 2.0 \times 10^{-5} / \cos\left(\theta_{SOL}\right), \quad (2)$$

i.e., the reflectance resolution decreases with increasing solar zenith angle. For example, while OLI reflectance values are spaced 2.0×10^{-5} for $\theta_{SOL} = 0°$, reflectance spacing increases to 4.0×10^{-5} for $\theta_{SOL} = 60°$, resp. 7.7×10^{-5} for $\theta_{SOL} = 75°$.

2.1.3. Areas of interest

The GRCM scheme has been developed and tested using OLI subscenes from areas of interest (AOIs) encompassing a wide range of environmental conditions (**Table 2**).

Preprints (www.preprints.org) | NOT PEER-REVIEWED | Posted: 4 July 2022 doi:10.20944/preprints202207.0048.v1

Table 2. Areas of interest (AOI) used in the development of the GRCM scheme. Each AOI covers an area of ca. 24 × 36 km².

AOI designation	Geographical extension	WRS2 path / row	Elevation above MSL	Description	Remarks
Brest [BRS]	48.170-48.386 °N 4.700-4.214 °W	203 / 026 204 / 026	0 m	Estuary and coastal waters of varying degrees of turbidity, frequent occurrence of swell on the open Atlantic.	AERONET [17] station Brest_MF located within AOI.
Haifa Bay [HFA]	32.750-32.966 °N 34.714-35.100 °E	174 / 037 175 / 037	0 m	Inner Haifa Bay strongly impacted by anthropogenic activities (harbor), oligotrophic conditions offshore.	AERONET [17] station Technion_Haifa_IL located within AOI.
Lake Constance East [LCE]	47.450-47.666 °N 9.270-9.750 °E	194 / 027	395 m	Large (536 km²) oligotrophic lake in central Europe, densely populated shores, intensively used for recreational purposes.	
Lake Puma Yumco [LPY]	28.434-28.650 °N 90.215-90.574 °E	138 / 040	5,013 m	Large (280 km²) oligotrophic high mountain lake on the Qinghai-Tibet Plateau, significantly reduced Rayleigh optical depth.	

2.2 Processes controlling occurrence and intensity of sun glint

Sun glint in satellite imagery is caused by direct solar radiation impinging on sea surface facets oriented such that reflection into the satellite's field-of-view occurs. The more likely the occurrence of such facets, the more intense is the sun glint signal. The instantaneous distribution of the sea surface facets' orientation depends on multiple processes occurring at different spatial and temporal scales. The formation and orientation of small capillary waves is primarily driven by surface winds [6, 18], but also depends on atmospheric stability [19] as well as water temperature and density [20]. These small capillary waves form upon the underlying swell modifying the orientation of surface facets. The sea surface roughness is further influenced by the presence of currents [21], internal waves [22], as well as upwelling or mixing of water masses [23]. Biological activity or oil slicks may lead to the creation of surface films which will damp surface roughness [24]. Other processes of potential relevance include presence of slush, or sub-surface topography [25]. Many of these processes are highly variable in space and time over a wide range of scales, which is why correction methods aiming at assessing the sun glint intensity from external information (e.g., surface wind) often have not provided the desired results. This is especially true for high resolution imagery where small-scale resp. short-term processes do not average out over the area represented by an individual pixel.

Sea surface facets constitute an interface between two dielectric media, i.e. (sea) water and air. Reflection and transmission of light at/through these facets depend on the ratio of the medias' refractive indices as well as the angle of light incidence and are quantified by the Fresnel equations [26]. As the refractive index of water depends on wavelength, salinity, and temperature (for example $n \cong 1.337$ for sea water at 15.0 °C, 35.0 PSU, and 700 nm) [27], so do reflectance and transmittance of light at/through the water surface. As shown by [4], the wavelength dependence of the refractive index of water leads to a significant increase of the glint reflectance from the SWIR towards shorter wavelengths (see Section 4.5). The dependence of the refractive index of water on salinity and temperature variations is much smaller for the applicable ranges [4] and is not considered herein.

Preprints (www.preprints.org) | NOT PEER-REVIEWED | Posted: 4 July 2022 doi:10.20944/preprints202207.0048.v1

2.3. Estimating the impact of sun glint on water constituent retrieval

An important aspect of sun glint is that it negatively affects the accuracy of water constituent retrieval schemes as demonstrated exemplarily below for chlorophyll (CHL) and total suspended matter (TSM).

2.3.1. Impact of sun glint on chlorophyll retrieval

To assess the impact of sun glint on chlorophyll retrieval, OC2 has been selected as a simple, yet representative retrieval scheme [28]: representative, because it is based on a blue/green ratio (BGR) approach like many other CHL retrieval schemes; simple, because only two spectral bands are used:

$$\log_{10}(CHL) = a_0 + a_1\chi + a_2\chi^2 + a_3\chi^3 + a_4\chi^4, \quad (3)$$

where CHL is the chlorophyll-a concentration [mg m^{-3}], and χ is defined as the common logarithm of the BGR of the remote sensing reflectance R_{RS}^{0+} [sr^{-1}] just above the sea surface:

$$\chi = \log_{10}\left(\frac{R_{RS}^{0+}(\lambda_{blue})}{R_{RS}^{0+}(\lambda_{green})}\right). \quad (4)$$

In the case of OC2 for MODIS (OC2M), λ_{blue} and λ_{green} represent MODIS bands 10 (0.483-0.493 µm) and 12 (0.546-0.556 µm), whereas the coefficients $a_{0,\ldots,4}$ adopt the values 0.2500, -2.4752, 1.4061, -2.8233, and 0.5405, respectively [29].

Equations (3) and (4) have been used to estimate the impact of sun glint on CHL retrieval accuracy for oligotrophic (CHL = 0.05 mg m^{-3}), mesotrophic (CHL = 0.5 mg m^{-3}), and eutrophic (CHL = 5.0 mg m^{-3}) waters, the trophic states defined herein as in [30] for the marine environment, i.e., mesotrophic for CHL within the range 0.1 to 1.0 mg m^{-3}, oligotrophic below, eutrophic above. The curves shown in **Figure 1 (a)** are derived as follows:

1. First, the BGR corresponding to the target CHL concentrations (0.05, 0.5, 5.0 mg m^{-3}) is determined, their values amounting to 4.07, 1.74, and 0.689, respectively.
2. $R_{RS}^{0+}(\lambda_{blue})$ is assumed to adopt a constant value of 0.005 sr^{-1}; a simplification motivated by the fact that the reflectance of Case-1 waters does not strongly depend on CHL at wavelengths around 500 nm [31].
3. $R_{RS}^{0+}(\lambda_{green})$ is then calculated by entering $R_{RS}(\lambda_{blue})$ into the corresponding BGR from step 1 for each of the three chlorophyll concentrations.
4. Finally, sun glint $R_{RS,SUG}$ ranging from 0.0 to 0.02 [sr^{-1}] is added to $R_{RS}^{0+}(\lambda_{blue})$ and $R_{RS}^{0+}(\lambda_{green})$. To simplify matters, it is assumed here that $R_{RS,SUG}$ is identical in both channels.

Figure 1 (a) shows that sun glint leads to significant CHL overestimation in oligotrophic waters. The (relative) overestimation is reduced for increasing CHL up to a switch point where BGR equals 1 (orange, equivalent to CHL ~1.8 mg m^{-3} for the simplified approach presented herein), beyond which sun glint leads to CHL underestimation.

Preprints (www.preprints.org) | NOT PEER-REVIEWED | Posted: 4 July 2022 doi:10.20944/preprints202207.0048.v1

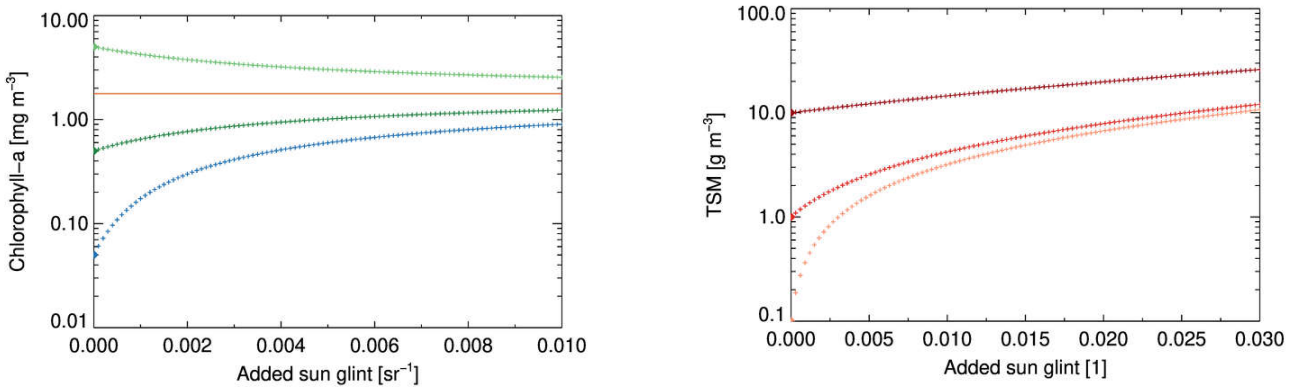

(**a**) (**b**)

Figure 1. (a) CHL retrieval error as a function of sun glint for the OC2M retrieval algorithm for oligotrophic waters (blue, CHL = 0.05 mg m^{-3}), mesotrophic waters (dark green, CHL = 0.5 mg m^{-3}), and eutrophic waters (light green, CHL = 5.0 mg m^{-3}). The orange line indicates the CHL concentration for a BGR of 1.0 which is independent of the sun glint contribution under the assumptions made herein (see main text); **(b)** Error of TSM retrieval [32] as a function of sun glint at λ = 655 nm for clear water (orange, TSM = 0.1 g m^{-3}), turbid water (light red, TSM = 1.0 g m^{-3}), and highly turbid water (dark red, TSM = 10.0 g m^{-3}). Note that the reflectance units differ between the two algorithms, OC2M being based on remote sensing reflectances R_{RS} while the TSM algorithm applies reflectance units ϱ.

2.3.2. Impact of sun glint on total suspended matter retrieval

The sun glint induced retrieval error can become significantly larger for algorithms based on absolute reflectances instead of reflectance ratios (where the impact of sun glint cancels out to a certain degree). An example for this is the total suspended matter (TSM) algorithm by [32]:

$$TSM = \frac{A^{\rho} \times \rho_w}{1 - \rho_w / C^{\rho}} \text{ [g m}^{-3}\text{]}, \quad (5)$$

where ρ_w is the water leaving reflectance [1], and A^{ρ} and C^{ρ} are wavelength dependent empirically derived coefficients amounting to $A^{\rho} = 289.29$ [g m^{-3}] and $C^{\rho} = 0.1686$ [1] at a wavelength of 0.655 µm representative of OLI band B4 (0.64-0.67 µm).

Figure 1 (b) shows the sun glint induced TSM retrieval error according to Equation (5) for clear (TSM = 0.1 g m^{-3}), turbid (TSM = 1.0 g m^{-3}), and very turbid (TSM = 10.0 g m^{-3}) waters. Similar as for CHL, TSM retrieval accuracy is relatively strongest affected by sun glint in clear waters, leading to substantial overestimation. In contrast to OC2M, there is no switch point, increasing sun glint is always leading to increasing TSM retrieval errors.

2.3.3. Indicative sun glint thresholds to meet specific accuracy requirements

Table 3 shows the relative errors caused by the occurrence of sun glint when applying the simple CHL and TSM retrieval schemes presented in Sections 2.3.1. and 2.3.2. above. Note that sun glint is specified therein in reflectance units ϱ for both retrieval schemes, since this is the standard parameter calculated from Landsat 8 OLI instrument counts (see Section 2.1.2). These relative errors can be used to set indicative threshold values beyond which sun glint correction is required to reach specific accuracy goals. For example, if the sun glint induced error to CHL retrieval is not to exceed 50% at CHL = 0.5 mg m^{-3}, sun glint contamination must not exceed ca. 0.005 when applying the OC2M retrieval scheme.

Preprints (www.preprints.org) | NOT PEER-REVIEWED | Posted: 4 July 2022 doi:10.20944/preprints202207.0048.v1

Table 3. Relative retrieval errors caused by the occurrence of sun glint (in reflectance units) for selected CHL and TSM concentrations applying the simple models described in Sections 2.3.1. and 2.3.2. Sun glint levels leading to a relative error of ≥ 2, respectively ≤ 0.5, are highlighted yellow, resp. green.

Sun glint	0.0001	0.0002	0.0005	0.001	0.002	0.005	0.01	0.02	0.05
CHL = 0.05 mg/m³	1.07 E+0	1.14 E+0	1.35 E+0	1.73 E+0	2.53 E+0	4.99 E+0	8.64 E+0	1.40 E+1	2.22E+1
CHL = 0.5 mg/m³	1.01 E+0	1.02 E+0	1.05 E+0	1.10 E+0	1.20 E+0	1.44 E+0	1.76 E+0	2.18 E+0	2.75 E+0
CHL = 5.0 mg/m³	0.99 E+0	0.99 E+0	0.97 E+0	0.94 E+0	0.89 E+0	0.79 E+0	0.68 E+0	0.57 E+0	0.46 E+0
TSM = 0.1 g/m³	1.29 E+0	1.58 E+0	2.46 E+0	3.92 E+0	6.88 E+0	1.60 E+1	3.19 E+1	6.69 E+1	2.08 E+2
TSM = 1.0 g/m³	1.03 E+0	1.06 E+0	1.15 E+0	1.30 E+0	1.61 E+0	2.55 E+0	4.20 E+0	7.85 E+0	2.26 E+1
TSM = 10.0 g/m³	1.00 E+0	1.01 E+0	1.02 E+0	1.04 E+0	1.09 E+0	1.22 E+0	1.45 E+0	1.98 E+0	4.27 E+0

2.4. Morphological aspects of sun glint

2.4.1. Visual appearance of sun glint in high resolution imagery

Sun glint is characterized in near-nadir high resolution imagery by specific reflectance patterns, exemplarily shown here at the example of an OLI scene covering the coastal waters in the Brest AOI (**Figure 2**). Filament-like structures of low reflectance are observed within high reflectance areas, indicating locally lower surface roughness (e.g., near x/y position 800/100). Another typical sun glint pattern is produced by swell, characterized by increased sun glint parallel to the wave trains (e.g., near x/y position 100/50). These sun glint specific spatial patterns differ significantly from the typically much smoother reflectance patterns caused by atmospheric or oceanic processes.

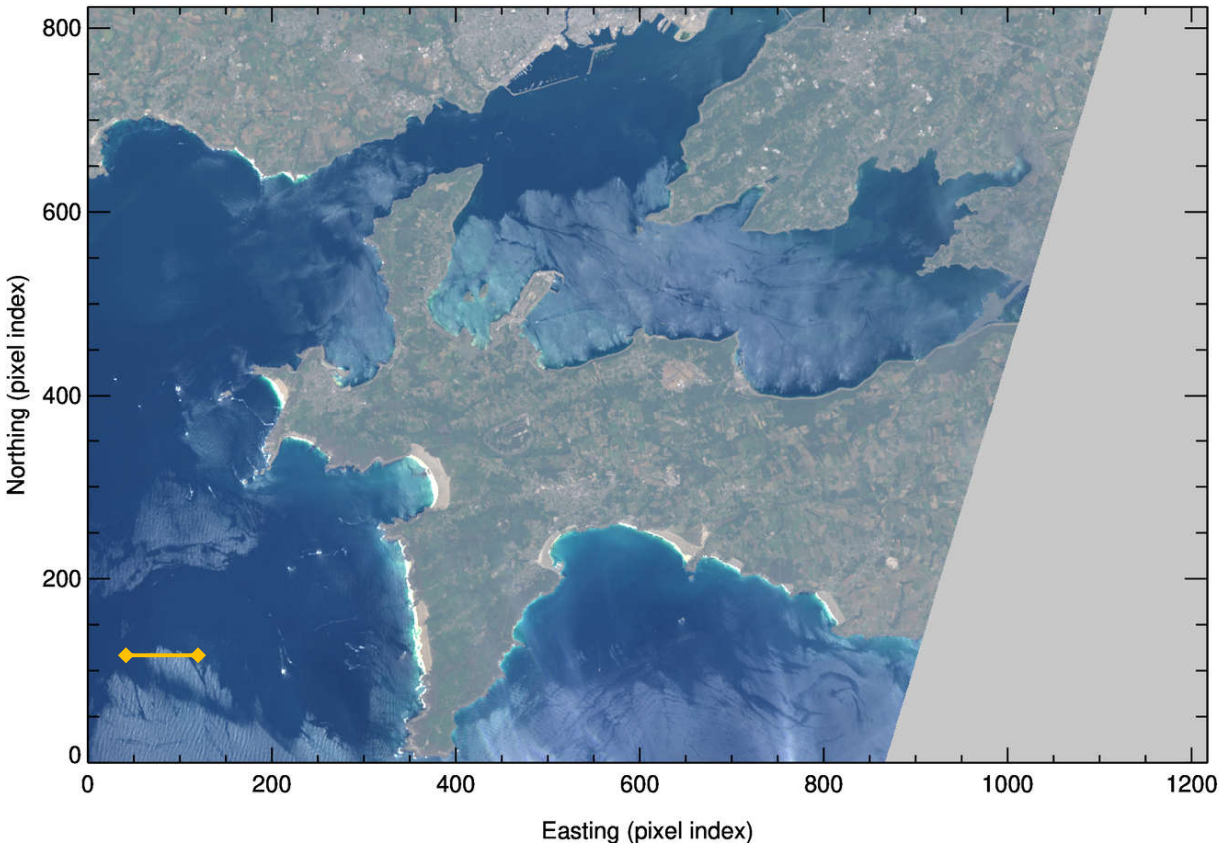

Figure 2. Contrast-enhanced near-true-color image of the Brest AOI (Table 2) derived from OLI product LC08_L1TP_204026_20200623_20200823_C2_T1 acquired on 23 June 2020 at 11:11 UTC using channels B2, B3, and B4. The yellow line in the lower left indicates the position of the transect analyzed in Figure 3. The grey area on the right has not been covered by the OLI scene.

Preprints (www.preprints.org) | NOT PEER-REVIEWED | Posted: 4 July 2022 doi:10.20944/preprints202207.0048.v1

2.4.2. Pixel-to-pixel reflectance contrast

Aside the larger sun glint features spreading over several pixels, sun glint is also characterized by significantly increased pixel-to-pixel reflectance contrast (PPRC) at TOA as compared to glint free areas. **Figure 3 (a)** shows the TOA reflectance for OLI channels B3, B5, and B7 along the transect indicated in Figure 2, extending from areas of low glint (ρ^{TOA} $(B7) < 0.005$) to areas of high glint (ρ^{TOA} $(B7) \approx 0.04$), and back to areas of low glint. While the corresponding PPRC depicted in **Figure 3 (b)** is small in the glint-free areas ($|\mathrm{PPRC}| < 0.001$), it strongly varies in glint affected areas where is reaches values of $|PPRC| > 0.02$.

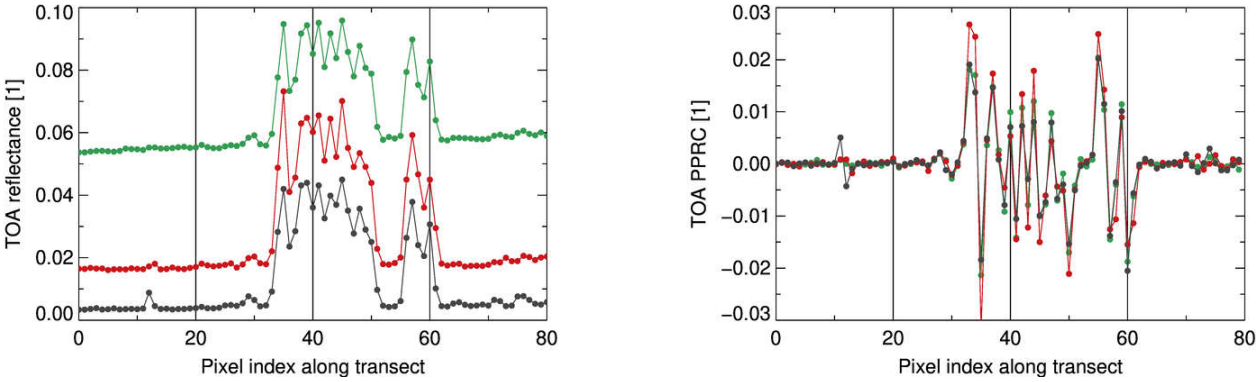

(**a**) (**b**)

Figure 3. (a) TOA reflectance; **(b)** Pixel-to-pixel reflectance contrast for OLI channels B3 (green), B5 (red), and B7 (dark grey) along the transect (40/120 to 120/120) indicated in **Figure 2**.

The following conclusions can be drawn from the visualization of the sun glint's specific morphological characteristics depicted in **Figure 3**: First, OLI's spatial resolution of 30 m is sufficient to resolve reflectance patterns caused by sun glint. Second, there is no significant spatial shift in the glint features between different OLI channels, i.e., all OLI channels observe the glint patterns in a very similar way (see for example the swell-induced local reflectance maxima between ca. pixels #35 to #50).

The PPRC is therefore considered a suitable measure to identify sun glint affected pixels in the SWIR as it is only little affected by the usually much smoother TOA reflectance patterns caused by atmospheric turbidity while there is no contribution from the water body itself at these wavelengths.

2.5. A sun glint mask derived from the local reflectance contrast in the SWIR

2.5.1. Identifying sun glint affected pixels

Based on the observation that sunglint is characterised in the SWIR by local reflectance contrasts stronger than those produced by atmospheric processes under cloud-free conditions, a procedure to identify the sun glint affected area from observations in OLI channel B7 has been devised. Note that the procedure only applies to pixels classified as suitable for sun glint correction (see Section 3.2.5).

First, the maximum reflectance contrast (MRC) is defined as a two-dimensional local contrast measure:

$$MRC \equiv mrc_{i,j} := \max_{\substack{i-1\le k\le i+1 \\ j-1\le l\le j+1}} \left(\rho^{TOA}_{k,l}(B_7) - \rho^{TOA}_{i,j}(B_7)\right). \quad (6)$$

In a second step, the mask MSK_{PGP} of potentially glinted pixels is created by applying a threshold THR_{PGP}:

$$MSK_{PGP} \equiv msk\_pgp_{i,j} := \begin{cases} 1 \text{ if } mrc_{i,j} > THR_{PGP}, \\ 0 \text{ otherwise}, \end{cases} \quad (7)$$

Preprints (www.preprints.org) | NOT PEER-REVIEWED | Posted: 4 July 2022 doi:10.20944/preprints202207.0048.v1

where THR_{PGP} needs to be chosen such that the contrast produced by environmental or instrumental noise is not mistaken for sun glint. (See Section 2.5.2. on how THR_{PGP} as well as the other threshold values introduced in this section are practically determined.)

Environmental conditions leading to sun glint are typically spreading over areas significantly larger than that represented by an individual OLI pixel. Sun glint affected pixels rarely come "alone", but rather congregate in glint prone areas. This reasoning leads to the following criterion to remove pixels that likely have erroneously been classified as being potentially glinted:

$$MSK_{GAP} \equiv msk\_gap_{i,j} := \begin{cases} 1 \text{ if } msk\_pgp_{i,j} = 1 \wedge \underset{\mathrm{M\times M}}{\mathrm{mean}}\left(msk\_pgp_{i,j}\right) > THR_{GAP}, \\ 0 \text{ otherwise,} \end{cases} \quad (8)$$

i.e., a pixel classified as potentially glinted according to Equation (7) is considered being an actually glint affected pixel $msk\_gap_{i,j}$ if the coverage by potentially glinted pixels $msk\_pgp_{i,j}$ within the surrounding $M \times M$ window exceeds threshold THR_{GAP}.

Not all glinted pixels are characterized by a strong contrast against their neighbors, for example if the latter are similarly glinted, meaning that Equation (8) cannot be used to identify glint affected pixels in their entirety. A pixel $\rho_{i,j}^{TOA}$ is therefore considered to be located in a glint affected area (GAA) if the coverage of glint affected pixels (GAP) within an $N \times N$ window around it exceeds a threshold value THR_{GAA}:

$$MSK_{GAA} \equiv msk\_gaa_{i,j} := \begin{cases} 1 \text{ if } \underset{\mathrm{N\times N}}{\mathrm{mean}}\left(msk\_gap_{i,j}\right) > THR_{GAA}, \\ 0 \text{ otherwise,} \end{cases} \quad (9)$$

2.5.2. Determining the model parameters for the sun glint mask

In order to identify the glint affected area (GAA) by applying the method devised in Section 2.5.1, the threshold values THR_{PGP}, THR_{GAP}, THR_{GAA}, as well as the window widths M and N need to be determined.

For the threshold contrast value THR_{PGP}, i.e., the MRC value above which a pixel is considered as potentially glinted, this has been done as follows:

- Eight low cloud cover OLI scenes were preselected, encompassing otherwise a wide range of environmental conditions.
- Within each scene, one cloud-free area of negligible glint occurrence was determined from visual inspection.
- For each area, the 99th percentile $P_{99}$of the maximum reflectance contrast $mrc_{i,j}$ in channel B7 was calculated according to Equation (6).

Figure 4 presents the MRC P_{99} values for the eight glint-free areas as a function of the solar zenith, together with a fit representing THR_{PGP} by:

$$THR_{PGP}(\theta_{sol}) = 0.0005 \,/\, cos\,(0.95 \times \theta_{sol}). \quad (10)$$

The dependence of THR_{PGP} on the solar zenith angle is due to the fact that the reflectance change per unit Level-1 pixel value increases with increasing solar zenith according to Equation (2).

Preprints (www.preprints.org) | NOT PEER-REVIEWED | Posted: 4 July 2022 doi:10.20944/preprints202207.0048.v1

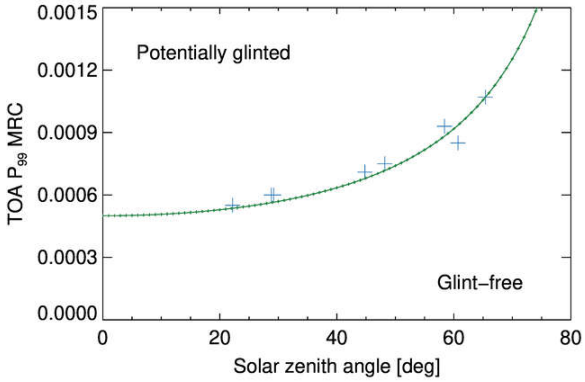

Figure 4. P99 of the maximum reflectance contrast $mrc_{i,j}$ in OLI channel B7 for eight glint free areas as a function of the solar zenith angle. The fit represents the threshold THR_{PGP} for the maximum contrast $mrc_{i,j}$ above which a pixel is considered potentially sun glint affected.

The window widths M and N as well as the threshold values THR_{GAP} and THR_{GAA} have been chosen as:

$$\begin{aligned} M &= 5, \\ THR_{GAP} &= (1+4)/M^2 = 0.2, \\ N &= 3, \\ THR_{GAA} &= 1/N^2 \cong 0.11, \end{aligned} \tag{11}$$

based on the following reasoning:

- A potentially glinted pixel $msk\_pgp_{i,j}$ is considered glint affected if at least four further pixels within a 5×5 window are also potentially glinted, hence $THR_{GAP} = (1 + 4)/25 = 0.2$.
- Any pixel (whether glint affected or not) is considered part of a glint affected area (GAA) if at least one glint affected pixel (GAP) is located within any 3×3 window, hence $THR_{GAA} = 1/9 \cong 0.11$.

These values represent pragmatic solutions based on practical experience. They likely need to be chosen differently for sensors other than OLI to provide reliable results.

2.6 Contrast-based sun glint estimation

2.6.1 The light field at TOA in the VNIR and SWIR above water

Under cloud-free conditions, the top-of-atmosphere radiance L^{TOA} above water can be decomposed as follows [5]:

$$L^{TOA} = L^{TOA}_{RAY} + L^{TOA}_{AER} + L^{TOA}_{AR} + T\,L^{0+}_{SUG} + t\,L^{0+}_{WCP} + t\,L^{0+}_{WAT}, \tag{12}$$

where L^{TOA}_{RAY} and L^{TOA}_{AER} designate the contributions of Rayleigh (including sky glint) and aerosol scattering to the TOA radiance respectively, while L^{TOA}_{AR} is a coupling term accounting for the interaction between aerosol and Rayleigh scattering; L^{0+}_{SUG} is the sun glint just above the sea surface, attenuated on its way to the sensor by the direct atmospheric transmittance T, whereas L^{0+}_{WCP} and L^{0+}_{WAT} represent the contributions from white caps and the water leaving radiance just above the sea surface, subsequently attenuated by the diffuse atmospheric transmittance t. Note that all parameters in Equation (12) depend on wavelength and observation geometry, indicated only if required to enhance comprehensibility.

In the SWIR, the terms L^{TOA}_{RAY}, L^{0+}_{AR}, L^{0+}_{WCP}, and L^{0+}_{WAT} are very small since the atmospheric Rayleigh optical depth is very low and the absorption of pure water is very high, [12, 33, 34] and can reasonably be omitted such that Equation (12) simplifies to:

Preprints (www.preprints.org) | NOT PEER-REVIEWED | Posted: 4 July 2022 doi:10.20944/preprints202207.0048.v1

$$L^{TOA}(\lambda_{SWIR}) = L^{TOA}_{AER}(\lambda_{SWIR}) + T(\lambda_{SWIR}) \times L^{0+}_{SUG}(\lambda_{SWIR}). \quad (13)$$

Introducing:

$$T(\lambda_{SWIR}) \times L^{0+}_{SUG}(\lambda_{SWIR}) = L^{TOA}_{SUG}(\lambda_{SWIR}), \quad (14)$$

Equation (13) can be rearranged to:

$$L^{TOA}_{SUG}(\lambda_{SWIR}) = L^{TOA}(\lambda_{SWIR}) - L^{TOA}_{AER}(\lambda_{SWIR}), \quad (15)$$

i.e., once the aerosol contribution to the TOA radiance is known, the sun glint contribution at TOA can be isolated. Dividing Equation (15) by the factor E^{TOA}_d/π, where E^{TOA}_d is the downwelling irradiance at TOA, one obtains the equivalent formulation in reflectance units ρ:

$$\rho^{TOA}_{SUG}(\lambda_{SWIR}) = \rho^{TOA}(\lambda_{SWIR}) - \rho^{TOA}_{AER}(\lambda_{SWIR}). \quad (16)$$

2.6.2 Pattern-based sun glint identification

The spectral dependence of the sun glint reflectance at TOA can be expressed as

$$\rho^{TOA}_{SUG}(\lambda) = c(\lambda_{SWIR}, \lambda) \times \rho^{TOA}_{SUG}(\lambda_{SWIR}), \quad (17)$$

where $c(\lambda_{SWIR}, \lambda)$, further on referred to as TOA Spectral Glint Conversion factor (TSGC), is a scalar factor quantifying the glint reflectances at target wavelength λ relative to the reference wavelength λ_{SWIR}.

In principle, c varies across a satellite scene as it depends on both observation geometry and atmospheric transmittance (see Section 2.7). To allow for the application of the GRCM scheme, c is considered constant over the entire (sub-)scene under consideration. This simplification is justified for the small AOIs considered herein and will normally lead to only minor over- or underestimation of the sun glint. Obviously, such simplification does not apply to inland waters at differing surface altitudes within a single scene. In this case, the water bodies need either to be treated independently, or a Rayleigh correction needs to be applied prior to glint correction.

As sun glint usually produces more contrasted patterns at TOA in cloud-free areas than do other atmospheric or oceanic processes, removing the sun glint pattern results in a contrast reduction; c is therefore chosen correctly if the total contrast within the sun glint corrected image $\rho^{TOA}_{COR}(\lambda)$ at the target wavelength, defined by:

$$\rho^{TOA}_{COR}(\lambda) = \rho^{TOA}(\lambda) - c(\lambda_{SWIR}, \lambda) \times \rho^{TOA}_{SUG}(\lambda_{SWIR}), \quad (18)$$

adopts a minimum:

$$c(\lambda_{SWIR}, \lambda) := \min_{c' \in [0, C']} f_c\left(\rho^{TOA}(\lambda) - c' \times \rho^{TOA}_{SUG}(\lambda_{SWIR})\right), \quad (19)$$

where f_c is a suitable measure of contrast and $[0, C']$ represents a sensible range of values for c. The practical implementation of the GRCM scheme is described in Section 3.

2.7. Information content of the TSGC

Introducing the atmospheric direct transmission $T(\lambda, \mu)$, where μ indicates the cosine of the solar (μ_S), resp. the observational (μ_O) zenith angle, Equation (17) can be expressed in terms of sun glint reflectance just above the water surface ρ^{0+}_{SUG}:

$$\rho^{0+}_{SUG}(\lambda)\, T(\lambda, \mu_S)\, T(\lambda, \mu_O) = c(\lambda_{SWIR}, \lambda)\, \rho^{0+}_{SUG}(\lambda_{SWIR})\, T(\lambda_{SWIR}, \mu_S)\, T(\lambda_{SWIR}, \mu_O). \quad (20)$$

The glint reflectance just above the water surface ρ^{0+}_{SUG} is determined by the bidirectional reflectance distribution function (BRDF) of the rough water surface and varies as a

Preprints (www.preprints.org) | NOT PEER-REVIEWED | Posted: 4 July 2022 doi:10.20944/preprints202207.0048.v1

function of wavelength due to the spectral dependence of the refractive index of water. Introducing the spectrally normalized BRDF ε by:

$$\varepsilon(\lambda_{REF}, \lambda) = BRDF\ (\lambda)\ /\ BRDF(\lambda_{REF}), \tag{21}$$

and setting $\lambda_{REF} = \lambda_{SWIR}$, it follows that:

$$\rho_{SUG}^{0+}(\lambda) = \varepsilon(\lambda_{SWIR}, \lambda)\ \rho_{SUG}^{0+}(\lambda_{SWIR}). \tag{22}$$

The spectrally normalized BRDF ε has been determined by [4] using radiative transfer calculations. Setting the reference wavelength to 2190 nm, i.e., the central wavelength of L8 OLI's channel B7, it increases from 1.0 at 2190 nm to about 1.25 at 500 nm. It has also been shown by [4] that the dependence of ε on the observation geometry is small as compared to its spectral variation for predominantly nadir looking instruments. Introducing Equation (22) into Equation (20) gives:

$$c(\lambda_{SWIR}, \lambda) = \varepsilon(\lambda_{SWIR}, \lambda)\ \frac{T(\lambda,\mu_S)\,T(\lambda,\mu_O)}{T(\lambda_{SWIR},\mu_S)\,T(\lambda_{SWIR},\mu_O)}. \tag{23}$$

Knowing both the parameters c and ε allows to deduce information on the spectral dependence of the atmospheric transmission (and hence optical depth) against a reference wavelength, as already stated by [35] and further discussed in Section 4.5.

3. Practical implementation of the glint correction scheme

The flow chart in **Figure 5** provides a top-level description of the practical implementation of the GRCM scheme. The individual processing steps are indicated by the letters [A] to [H], outlined in more detail in the following subsections, and applied to the sample scene shown in **Figure 2** for illustration purposes.

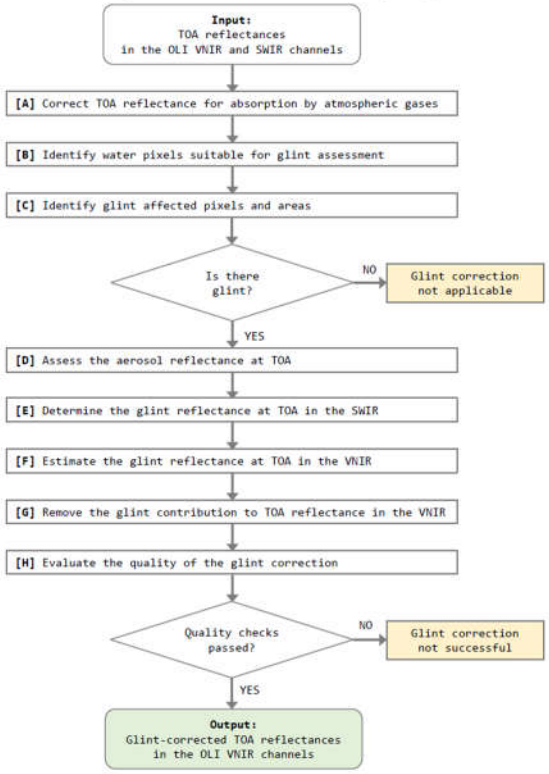

Figure 5. Flow chart of the proposed sun glint correction scheme.

3.1 [A] Correct the TOA reflectance for absorption by atmospheric gases

The atmospheric absorption due to CO_2, H_2O, O_2, and O_3 cannot be neglected for certain OLI channels. Its impact on TOA reflectance can reasonably well be determined by assuming gaseous absorption taking place above the top of the scattering atmosphere:

Preprints (www.preprints.org) | NOT PEER-REVIEWED | Posted: 4 July 2022 doi:10.20944/preprints202207.0048.v1

$$\rho^* = \rho^{TOA}/(T^*_{CO2}\, T^*_{O2}\, T^*_{O3}\, T^*_{H2O}), \tag{24}$$

where T^* is the double path gaseous transmittance, and ρ^* designates the TOA reflectance corrected for atmospheric gaseous absorption.

In the present work, atmospheric gaseous transmittance has been calculated using the SMAC (Simplified Method for Atmospheric Correction) approach [36]. The required band-specific coefficients for the OLI instrument have been taken from [37], while the atmospheric parameters (total column ozone, total column water vapor, mean sea level atmospheric pressure) are taken from ERA5 hourly data on single levels [38].

3.2 [B] Identify water pixels suitable for glint assessment

There are a number of environmental conditions with a potential to negatively impact the GRCM scheme, most importantly the presence of clouds and cloud shadows, but also white caps, bottom-up effects in shallow waters, etc. While some of these processes do not significantly affect reflectances in the NIR and SWIR due the strong absorption of light in water at these wavelengths, they have a significant potential to "confuse" contrast minimization in the VIS. The concerned pixels therefore need to be excluded from further processing.

Cloud screening: In the context of the present study, visual inspection using all OLI channels (including the Cirrus channel B9 and the thermal infrared (TIR) channels B10 and B11) has been applied to avoid the presence of clouds and cloud shadows in the investigated areas of interest.

Dynamic water mask: A normalized difference water index (NDWI) defined by:

$$\text{NDWI} = \big(\rho^*(B7) - \rho^*(B3)\big)/\big(\rho^*(B7) + \rho^*(B3)\big), \tag{25}$$

is applied to identify water pixels. Similar indices have proven successful in identifying water surfaces in satellite imagery [39]. The NDWI defined through Equation (25) usually adopts values below -0.5 at TOA above water, while being positive above land surfaces. In the presence of sun glint, the NDWI above water increases, but remains negative. Therefore, the water mask (MSK_{WAT}) is defined herein as:

$$MSK_{WAT} \equiv msk\_wat_{i,j} := \begin{cases} 1 \text{ if } ndwi_{i,j} < THR_{WAT}, \\ 0 \text{ otherwise,} \end{cases} \quad \text{with } THR_{WAT} = -0.2. \tag{26}$$

Bright pixel mask: Pixels affected by objects on the water such as vessels, platforms, etc. need to be excluded as the corresponding sharp contrasts in the SWIR may erroneously be identified as sun glint. A simple empirical threshold approach is applied to identify such pixels:

$$MSK_{BGT} \equiv msk\_bgt_{i,j} := \begin{cases} 1 \text{ if mean } \big(\{\rho^*_{i,j}(B3), \rho^*_{i,j}(B5), \rho^*_{i,j}(B7)\}\big) < THR_{BGT}, \\ 0 \text{ otherwise,} \end{cases} \quad \text{with } THR_{BGT} = 0.08. \tag{27}$$

The bright pixel mask also identifies natural processes potentially disturbing the contrast minimization at VIS wavelengths such as the surf zone along the shore or the presence of highly turbid waters.

Coastal buffer: Water pixels close to the coastline are also excluded from further analysis to avoid the presence of water-land mixed pixels. A five-pixel buffer has been applied to the dynamic water mask MSK_{WAT} to provide the coastal buffer mask MSK_{BUF}.

Identification of pixels suitable for sun glint correction: The above defined masks are combined to identify pixels MSK_{GOOD} suitable for the application of the GRCM scheme ($\wedge$: logical AND, $\neg$: logical NOT):

Preprints (www.preprints.org) | NOT PEER-REVIEWED | Posted: 4 July 2022 doi:10.20944/preprints202207.0048.v1

$$MSK_{GOOD} \equiv msk\_good_{i,j} := MSK_{WAT} \wedge (\neg MSK_{BGT}) \wedge (\neg MSK_{BUF}). \quad (28)$$

3.3 [C] Identify glint affected pixels and areas

The practical application of the stepwise identification of glint affected areas as described in section 2.5 is depicted **Figure 6** for the Brest AOI. Of all pixels classified as water according to Equation (26), 87.9% are assessed suitable ("good") according to Equation (28) for use in the GRCM scheme. The maximum reflectance contrast (MRC) in OLI channel B7 calculated from Equation (6) is used to identify the glint affected pixels (GAP) according to Equation (8), covering 56.7% of all suitable pixels, finally resulting in a glint affected area (GAA) according to Equation (9) covering 72.1%.

If no sun glint is detected in an image, the glint contribution is set to zero and glint processing stops.

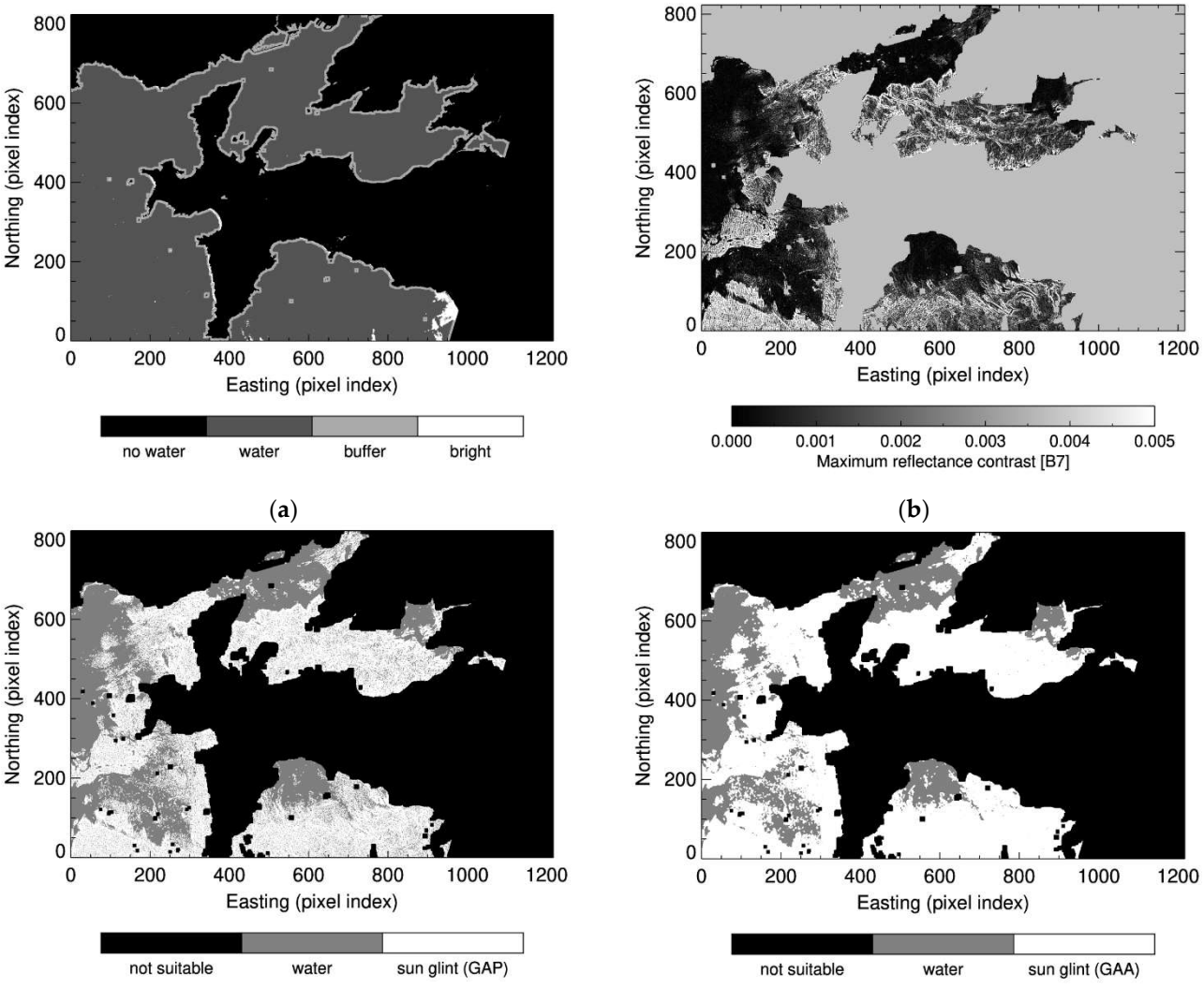

Figure 6. Determining the extension of the glint affected area (GAA) at the example of the Brest sample scene. (**a**) Identification of pixels suitable for use in the GRCM scheme; (**b**) TOA maximum reflectance contrast for OLI channel B7; (**c**) Glint affected pixels; (**d**) Glint affected area. See text for further details.

3.4 [D] Assess the TOA aerosol reflectance in the SWIR

In order to calculate the sun glint contribution ρ^*_{SUG} to the total TOA reflectance ρ^* in the SWIR according to Equation (16), the corresponding aerosol contribution

Preprints (www.preprints.org) | NOT PEER-REVIEWED | Posted: 4 July 2022 doi:10.20944/preprints202207.0048.v1

ρ^*_{AER} needs to be assessed. This is done by calculating the P_1 percentile in OLI channel B7 of all pixels considered as not being glint affected:

$$\rho^*_{AER}(B7) = P_1\{\rho^*(B7) \mid MSK_{GOOD} \wedge (\neg\, MSK_{GAP})\}. \quad (29)$$

The SWIR aerosol reflectance defined through Equation (29) is applied to the entire AOI; it is not attempted to assess the spatial variability of the aerosol reflectance within the scene. For the Brest AOI, $\rho^*_{AER}(B7)$ amounts to 0.0031, indicating rather low atmospheric turbidity.

3.5. [E] Determine the TOA glint reflectance in the SWIR

Having determined $\rho^*_{AER}(B7)$, the TOA glint reflectance in the SWIR is obtained by applying Equation (16):

$$\rho^*_{SUG}(B7) := \begin{cases} \rho^*(B7) - \rho^*_{AER}(B7) \text{ if } \rho^*(B7) \geq \rho^*_{AER}(B7), \\ 0 \text{ otherwise.} \end{cases} \quad (30)$$

3.6. [F] Estimate the TOA glint reflectance in the VNIR

Once $\rho^*_{SUG}(B7)$ is known, it can be used to estimate the TSGC factor c as described in section 2.6:

$$c(B7, B_i) := \min_{c' \in [0,1.5]} (f_c\,[\rho^*(B_i) - c' \times \rho^*_{SUG}(B7)]), \quad (31)$$

where B_i is the OLI channel to be sun glint corrected, f_c is chosen as the average maximum reflectance contrast over the entire glint affected area (GAA), further on referred to as AMRC, and c' is varied within the range from 0.0 to 1.5 which has shown sufficient to cover the combined spectral dependence on sun glint and atmospheric transmission for all OLI channels.

Figure 7 (a) demonstrates the contrast minimization procedure for the Brest AOI at the example of OLI channel B3 (0.562 µm): subtracting increasing portions of the SWIR sun glint contribution from the TOA reflectance $\rho^*_{SUG}(B3)$ leads to decreasing AMRC values until a minimum is reached at $c(B7, B3) = 0.96$, beyond which overcorrection sets in. The reduction of the average maximum reflectance contrast ($\Delta AMRC$) depends on sun glint intensity and amounts to $\Delta AMRC = 0.00157$ in OLI channel B3 for the sample Brest AOI. The corresponding values for the other OLI channels are found in **Table 4**.

3.7. [G] Remove the TOA glint contribution in the VNIR

Once the TSGC factor $c(B7, B_i)$ has been determined, the TOA reflectance in OLI channel B_i can be corrected for the sun glint contribution following Equation (18):

$$\rho^*_{COR}(B_i) = \rho^*(B_i) - c(B7, B_i) \times \rho^*_{SUG}(B7). \quad (32)$$

Note that this correction is applied to all pixels classified as water according to Equation (26).

The impact of the sun glint correction is demonstrated in **Figure 7 (b)** showing the mean TOA reflectance for OLI channels B2 to B6 before (solid line) and after (dashed line) sun glint correction for glint affected pixels (red) and neighboring pixels (distance ≤ 5 pixels) not classified as glint affected (blue). The amount of sun glint correction at TOA increases with increasing wavelength: while the average reflectance correction of glint affected pixels amounts to 0.0129 for OLI channel B2, it increases to 0.0203 for OLI channel B5, caused by increasing atmospheric transmission towards longer wavelengths. Indicating the success of the glint correction, the glint-corrected TOA reflectance does not differ significantly from the reflectance of neighboring non-glint affected pixels for all OLI channels.

The actual application of the sun glint correction is demonstrated in **Figure 7 (c)** and **(d)**, showing the TOA reflectance for the Brest AOI in OLI channel B3 before and after subtraction of the sun glint contribution. While sub-subsurface processes are obscured by

Preprints (www.preprints.org) | NOT PEER-REVIEWED | Posted: 4 July 2022 doi:10.20944/preprints202207.0048.v1

sun glint over large areas of the non-corrected image, the glint corrected TOA reflectance reveals a lot of detail about processes within the water body, well visible for example in the north-eastern estuaries.

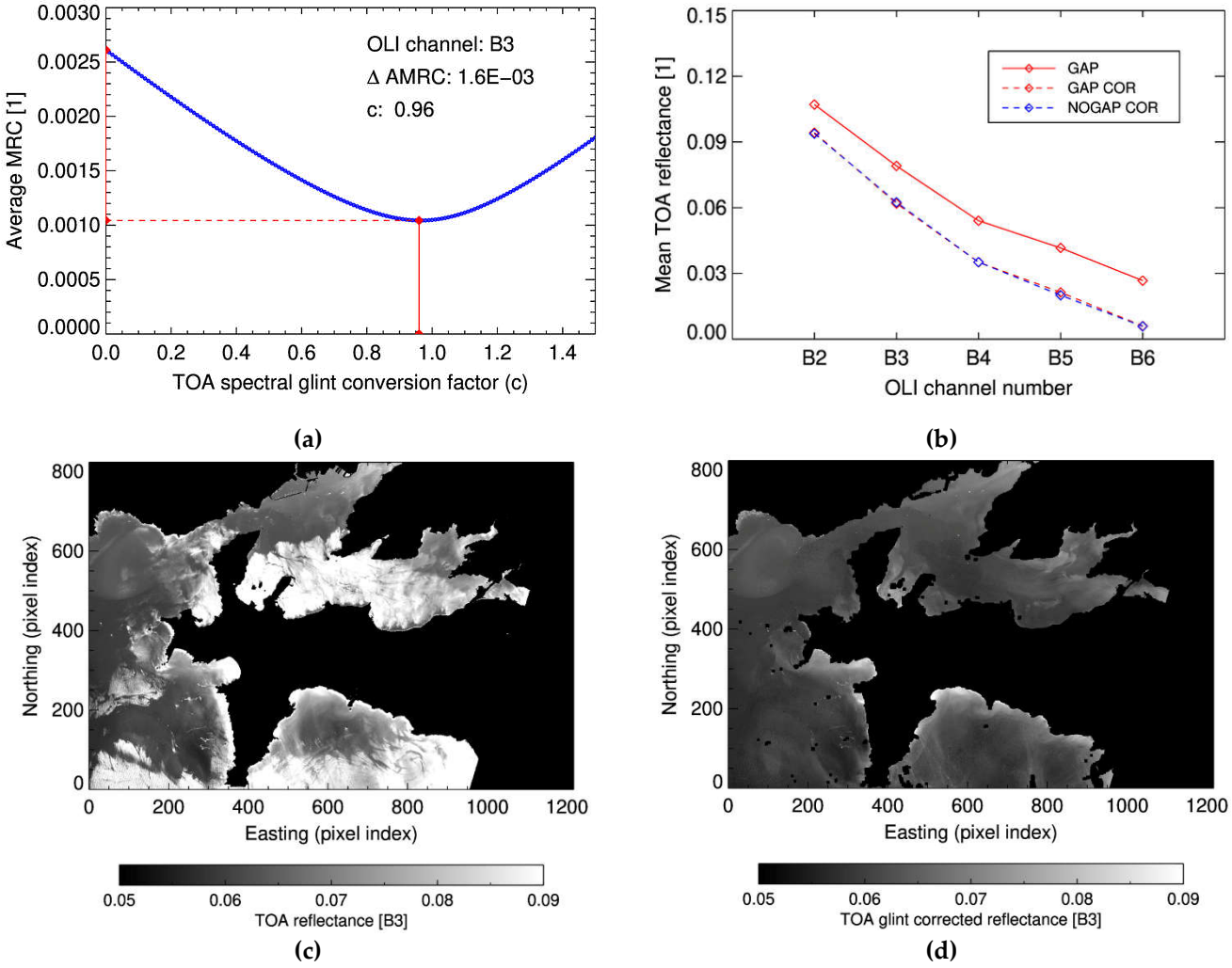

Figure 7. (a) Graphical representation of the minimization procedure to determine the TSGC factor *c* at the example of OLI channel B3 for the Brest sample area; **(b)** Mean TOA reflectance before and after glint correction for glint affected and neighboring less glint affected pixels; **(c)** TOA reflectance in OLI channel B3 before glint correction; **(d)** TOA reflectance in OLI channel B3 after applying the GRCM scheme. See text for further explanation.

3.8. Evaluate the quality of the glint correction [H]

The success of the glint correction procedure for a particular image can be assessed in a qualitative way through visual inspection: if previously obscured water-leaving reflectance patterns become visible after correction, a significant portion of the sun glint must have been removed, allowing for a better general understanding of the in-water biogeochemical processes, especially by experts with in-depth knowledge of the investigated area. If glint patterns persist, or if artefacts are created, then the correction was obviously less successful.

To assess the quality of the glint correction in a quantitative manner is more difficult. A number of metrics have been defined towards this aim:

TOA aerosol reflectance in the SWIR: The TOA aerosol reflectance in the SWIR $\rho^*_{AER}(B7)$ is required to isolate the glint reflectance. Values of $\rho^*_{AER}(B7) > \sim 0.005$ hint to either a high atmospheric aerosol load or the occurrence of non-negligible sun glint outside the glint affected area, the latter with potentially negative consequences on the GRCM scheme.

Preprints (www.preprints.org) | NOT PEER-REVIEWED | Posted: 4 July 2022 doi:10.20944/preprints202207.0048.v1

Average contrast reduction: The GRCM scheme relies on the occurrence of exploitable reflectance contrasts in the SWIR. In case the reduction of the average maximum reflectance contrast (Section 3.6) adopts values of $\Delta AMRC < \sim 2 \times 10^{-4}$, the glint signal may be insufficient to allow for an accurate determination of the TSGC factor $c(B7, B_i)$.

Similarity of average TOA reflectance in glint-free vs. glint-corrected areas: Assuming sun glint being only loosely correlated with the atmospheric and water leaving reflectance, the average reflectance difference ΔREF between glint affected and neighboring non-glint affected pixels should be small after correction. Values of $|\Delta\text{REF}| > \sim 0.001$ may hint at low performance of the GRCM scheme for a particular scene and/or channel.

The indicative threshold values given above are based on practical experience. More complex quality evaluation schemes will have to be devised for the automated processing of larger amounts of images.

4. Discussion

4.1. Requirements on the observing imager

A number of requirements must be met by the observing imager to allow for the application of the GRCM scheme:

- The imager must be able to resolve morphological fine structures typical of sun glint, requiring a spatial resolution of ≤ ca. 50 m.
- The imager must dispose of at least one channel in the SWIR, preferably at wavelengths $\geq 2.0\ \mu m$ to avoid non-negligible sub-surface contributions for virtually all water types.
- All applied spectral channels need to provide approx. identical representations of the observed water surface in terms of observation time, spatial resolution, and image registration.

As of 2022, OLI onboard Landsat 8 as well as OLI-2 onboard Landsat 9 appear to be the operational instruments best matching the above conditions. The hyperspectral EnMap mission [40] successfully launched in April 2022 will likely also meet the requirements for application of the proposed method, offering 30 m spatial resolution for the spectral range from 420 to 2450 nm with only a short temporal delay between VNIR and SWIR observations of 88 ms. This is not the case for the MSI instrument onboard Sentinel 2A/B where VIS, NIR and SWIR channels operate at different spatial resolutions (10 m, 20 m, or 60 m) and, even more importantly, the different channels observe the same surface area with temporal delays of up to several seconds [41]; the rapidly changing sun glint patterns are therefore not identically represented in the different MSI channels. These issues might partly be overcome by applying averaging procedures at the price of reduced spatial resolution, but this has not been further investigated in this work.

4.2. Requirements on the environmental conditions

There are a number of environmental conditions with a potential to negatively affect the performance of the GRCM scheme. The single most important aspect in this respect concerns the presence of clouds potentially causing contrasts similar in intensity to sun glint. Conservative cloud masking is therefore mandatory. Similarly, pixels (partly) covered by objects on the water such as vessels, platforms, etc. need to be excluded.

Having the entire area of interest covered in sun glint will lead to an overestimation of the background aerosol reflectance in the SWIR and consequently to an underestimation of the glint signal. While a partial correction of glint patterns is still possible, leading to an enhanced visibility of sub-surface processes, the resulting glint-corrected TOA reflectance is too high and cannot be used for e.g., water constituent retrieval purposes. In case glint-free pixels are present in the vicinity of the aera of interest, this issue can possibly be overcome by increasing the size of the latter to also include those.

The scheme assumes horizontally homogeneous atmospheric conditions which may lead to artefacts due to local under- or overcorrection where the assumption does not hold.

Preprints (www.preprints.org) | NOT PEER-REVIEWED | Posted: 4 July 2022 doi:10.20944/preprints202207.0048.v1

This issue might be addressed by subdividing the area of interest into smaller sub-areas, but this in turn is limited by the need to have glint-free pixels in every sub-area.

The scheme does not provide reliable results if the glint signal is too weak or if the glint affected area covers only a very limited part of the image. In such cases, it should not be applied.

4.3. Practical application

The GRCM scheme has been applied to 15 OLI scenes from the years 2018 to 2022 experiencing glint affected areas exceeding 5%. A number of conclusions on strengths and weaknesses of the current implementation as well as suggestions for further improvements can be drawn from the retrieval statistics and quality metrics shown in **Table 4**.

There is excellent agreement in the retrieved TSGC factor c for a number of cases (e.g., LCE-2 vs. LCE-3; PYC-1 vs. PYC-2), pointing to the principal robustness of the retrieval scheme. Also, the average TOA reflectance after correction in high-glint areas is very similar to that of less-glinted areas (e.g., $|\Delta\mathrm{REF}\ (\mathrm{B3})| < 0.001$) for all open ocean site scenes (BRS, HFA) and also for two LCE inland water scenes, indicating that the sun glint induced TOA reflectance variability has been efficiently removed. On four occasions, $|\Delta\mathrm{REF}|$ adopts values > 0.001 for the inland water AOIs (LCE, LPY). This could indicate that sun glint is sometimes correlated with high water-leaving radiance, e.g., around river plumes characterized by highly turbid waters which prominently feature in both AOIs.

The TSGC factor c shows higher variability in OLI channel B2 than in the other channels which cannot fully be explained by the impact of the scene-specific differences in Rayleigh optical depth. This increased variability could indicate that the minimization process is disturbed by increased atmospheric Rayleigh scattering in channel B2 leading to contrast reduction at TOA and hence a reduction in the exploitable signal. Due to reduced atmospheric Rayleigh scattering, c is significantly higher for the high-mountain LPY scenes, especially in the VIS channels.

In two cases (HFA-2 and HFA-4), high glint coverage (GAA > 90%) is associated with high values of the SWIR reflectance at TOA ($\rho^{*}_{AER}(B7) > 0.01$), leading in one case (HFA-2) to a spectral dependence of c with an implausible maximum value in channel B3. Application of the GRCM scheme at high glint coverage is critical and should thus be excluded in automated processing.

Preprints (www.preprints.org) | NOT PEER-REVIEWED | Posted: 4 July 2022 doi:10.20944/preprints202207.0048.v1

Table 4. List of OLI scenes to which the GRCM scheme was applied, together with the corresponding retrieval statistics and quality metrics. The Landsat Product ID has been abbreviated: "LL" stands for "LC08_L1TP" (Landsat 8 Level 1 Terrain Precision), and "CT" stands for "02_T1" (Collection 2 Tier 1). Atmospheric surface pressure (p_srf) has been taken from ERA5 reanalysis [38], the solar zenith angle θ_S is taken from the OLI metadata file, and the quality parameters $\rho^*_{AER}(B7)$, $\Delta AMRC$ and ΔREF are described in Section 3.8.

AOI-ID	Landsat Product ID	p_srf [hPa]	θ_S [deg]	GAA [%]	ρ^*_{AER} (B7)	$\Delta AMRC$ (B3)	ΔREF (B3)	c (B2)	c (B3)	c (B4)	c (B5)	c (B6)
BRS-1	LL_203026_20190513_20200828_CT	1035	33.3	72	0.0044	0.00029	0.0003	0.71	0.92	0.98	1.00	1.04
BRS-2	LL_204026_20200404_20200822_CT	1017	45.6	100	0.0051	0.00109	0.0001	0.84	1.06	1.15	1.21	1.15
BRS-3	LL_204026_20200623_20200823_CT	1022	29.2	72	0.0031	0.00157	0.0005	0.72	0.96	1.06	1.14	1.16
BRS-4	LL_204026_20200810_20200918_CT	1014	36.9	78	0.0044	0.00039	0.0009	0.55	0.79	0.91	1.04	1.11
HFA-1	LL_175037_20220109_20220114_CT	1012	59.5	6	0.0030	0.00021	0.0002	0.55	0.76	0.83	0.91	0.90
HFA-2	LL_175037_20220415_20220420_CT	1015	30.7	100	0.0244	0.00091	0.0004	0.39	0.99	0.90	0.80	1.14
HFA-3	LL_174037_20220510_20220518_CT	1015	24.2	81	0.0054	0.00020	0.0004	0.61	0.87	0.89	0.89	0.95
HFA-4	LL_174037_20220526_20220602_CT	1016	22.0	99	0.0124	0.00037	0.0003	0.57	0.91	0.98	1.00	1.05
HFA-5	LL_174037_20220611_20220617_CT	1011	21.4	76	0.0080	0.00073	0.0006	0.85	1.02	1.11	1.17	1.12
LCE-1	LL_194027_20210722_20210729_CT	973	31.5	15	0.0031	0.00020	0.0008	0.46	0.65	0.78	0.96	1.09
LCE-2	LL_194027_20200601_20200824_CT	972	28.9	54	0.0008	0.00035	0.0008	0.75	0.97	1.04	1.09	1.10
LCE-3	LL_194027_20200719_20200911_CT	971	31.0	47	0.0006	0.00049	0.0029	0.74	0.99	1.08	1.15	1.16
LCE-4	LL_194027_20200820_20200905_CT	966	38.6	5	0.0007	0.00024	0.0018	0.68	0.93	1.05	1.11	1.12
LPY-1	LL_138040_20180706_20200831_CT	538	22.2	72	0.0054	0.00147	0.0027	1.09	1.19	1.25	1.25	1.13
LPY-2	LL_138040_20180908_20200831_CT	541	31.1	18	0.0003	0.00071	0.0055	1.09	1.17	1.22	1.22	1.10

4.4. Improving the accuracy of the minimization approach and widening its range of applications

The accuracy of the GRCM scheme could potentially be enhanced by the following measures:

- The GRCM scheme currently employs a relatively simple contrast measure to separate sun glint from background. Involving more complex pattern recognition methods (e.g., edge detection) might have a potential to further improve sun glint identification and quantification.
- In the current implementation, the SWIR aerosol reflectance at TOA and the TSGC factor c are determined in sequence. A two-dimensional minimization approach to determine both parameters simultaneously might prove beneficial, especially in scenes characterized by high glint cover.

It could further be explored in how far the proposed correction approach has potential to be applied beyond the correction of sun glint. Another potential application could concern the correction of thin cirrus over contrasted surfaces – involving contrast maximization in this case.

4.5. A potential contribution to atmospheric correction?

As stated in Section 2.7, the TSGC factor c inherently contains information on the spectral dependence of the atmospheric transmittance relative to a SWIR reference wavelength and hence also on the relative spectral dependence of the atmospheric optical depth (AOD). This is reflected by the increasing differences in the c values towards shorter wavelengths between e.g., the LPY and the LPC AOIs, the former characterized by a significantly lower Rayleigh optical depth due to its high-altitude location and a correspondingly higher atmospheric transmittance (see **Table 4**).

Expressing atmospheric transmittance as a function of optical depth and relative airmass, Equation (23) can be transformed to provide information on the difference in the aerosol optical depth in OLI channel B_i against the AOD τ_{AER} at the SWIR reference wavelength:

Preprints (www.preprints.org) | NOT PEER-REVIEWED | Posted: 4 July 2022 doi:10.20944/preprints202207.0048.v1

$$\Delta\tau_{AER} \equiv \tau_{AER}(B_i) - \tau_{AER}(B_7) = -\frac{\ln(c/\varepsilon \times \alpha)}{\left(\frac{1}{\mu_S}+\frac{1}{\mu_O}\right)}, \quad (33)$$

where the ratio α of the two-way Rayleigh transmittance in channel B_7 over channel B_i can be calculated from the atmospheric pressure [36], and ε is the spectrally normalized BRDF of the water surface as calculated and tabulated by [4].

Equation (33) has been tentatively applied to the Brest sample scene from 23 June 2020. The results shown in **Table 5** indicate a stronger spectral dependence for the GRCM-derived AOD as compared to the corresponding AOD daily averages from the nearby AERONET station Brest_MF [42], the latter interpolated to the central wavelengths of the OLI channels. For example, the AOD difference between channels B2 and B5 amounts to 0.12 for the AERONET observations, but to 0.39 if derived using Equation (33). There are several possible reasons for the observed discrepancies: the daily averaged AOD may not be representative of the conditions during the actual OLI overpass, the conditions at the AERONET site may not be representative of the conditions above the ocean, GRCM may not have been able to determine c with sufficient accuracy, or the Rayleigh transmittance ratio α may not have been correctly calculated.

Table 5. Estimation of the aerosol optical depth spectral dependence according to Equation (33) for the Brest sample scene from 23 June 2020 shown in Figure 2. See text for further details.

	B2	B3	B4	B5	B6
c	0.72	0.96	1.06	1.14	1.16
ε	1.27	1.25	1.23	1.21	1.13
α	0.70	0.83	0.90	0.97	1.00
$\Delta\tau_{AER}$	0.43	0.21	0.12	0.04	-0.01
AERONET τ_{AER}	~0.22	~0.18	~0.15	~0.10	~0.07

A thorough analysis beyond the scope of the present work is required to assess whether the TSGC factor c can indeed be derived from the GRCM scheme with sufficient accuracy to provide useful information for e.g., atmospheric correction purposes. At this point, it can just be concluded that sun glint at TOA is not only a source of noise that needs to be corrected in order to derive water constituent concentrations with reasonable accuracy, but also constitutes a potentially valuable source of information on spectral atmospheric properties.

Funding: This research received funding from ESA under contract 4000115822/15/I-SBo (SEOM S2-4Sci), the European Union's Horizon 2020 research and innovation programme under grant agreement No. 773421 (Nunataryuk), and the Israel Oceanographic and Limnological Research Ltd. under Purchase Orders PO22001889 and PO22001891.

Data Availability Statement: Landsat 8 Collection 2 Level 1 Tier 1 data courtesy of the U.S. Geological Survey. ERA5 hourly data on single levels from 1979 to present [38] was downloaded from the Copernicus Climate Change Service (C3S) Climate Data Store.

Acknowledgments: To be completed (anonymous reviewers, …)

Conflicts of Interest: The author declares no conflict of interest.

References

1. Sentinel-3 OLCI User Guide. Available online: https://sentinels.copernicus.eu/web/sentinel/user-guides/sentinel-3-olci (accessed on 20 June 2022).
2. Kay, S.; Hedley, J.D.; Lavender, S. Sun Glint Correction of High and Low Spatial Resolution Images of Aquatic Scenes: a Review of Methods for Visible and Near-Infrared Wavelengths. *Remote Sens.* **2009**, 1, 697-730. https://doi.org/10.3390/rs1040697.
3. Emberton, S.; Chittka, L.; Cavallaro, A.; Wang, M. Sensor Capability and Atmospheric Correction in Ocean Colour Remote Sensing, *Remote Sens.* **2016**, 8(1), 1-31. https://doi.org/10.3390/rs8010001.
4. Harmel, T.; Chami, M.; Tormos, T.; Reynaud, N.; Danis, P.-A. Sunglint correction of the Multi-Spectral Instrument (MSI)-SENTINEL-2 imagery over inland and sea waters from SWIR bands. *Remote Sens. Environ.* **2018**, 204, 308-321. https://doi.org/10.1016/j.rse.2017.10.022.

5. Wang, M.; Bailey, S. Correction of sun glint contamination on the SeaWiFS ocean and atmosphere products. *Appl. Opt.* **2001**, 40, 4790-4798. https://doi.org/10.1364/AO.40.004790.
6. Cox, C; Munk, W. Measurement of the Roughness of the Sea Surface from Photographs of the Sun's Glitter. *J. Opt. Soc. Am.* **1954**, 44, 838-850, https://doi.org/10.1364/JOSA.44.000838.
7. Hochberg, E.J.; Andrefouet, S.; Tyler, M.R. Sea surface correction of high spatial resolution Ikonos images to improve bottom mapping in near-shore environments. *IEEE Trans. Geosci. Remote Sens.* **2003**, 41(7), 1724-1729. https://doi.org/10.1109/TGRS.2003.815408.
8. Hedley, J.D.; Harborne, A.R.; Mumby, P.J. Technical note: Simple and robust removal of sun glint for mapping shallow - water benthos. *Int. J. Remote Sens.* **2005**, 26(10), 2107-2112. https://doi.org/10.1080/01431160500034086.
9. Hu, C. An empirical approach to derive MODIS ocean color patterns under severe sun glint. *Geophys. Res. Lett.* **2011**, 38(1), L01603. https://doi.org/10.1029/2010GL045422.
10. Zorrilla, N.A.; Vantrepotte, V.; Ngoc, D.D.; Huybrechts, N.; Gardel, A. Automated SWIR based empirical sun glint correction of Landsat 8-OLI data over coastal turbid water. *Opt Express* **2019**, 27(8), A294-A318. https://doi.org/10.1364/OE.27.00A294.
11. Steinmetz, F.; Deschamps, P.; Ramon, D. Atmospheric correction in presence of sun glint: application to MERIS. *Opt. Express* **2011**, 19, 9783-9800. https://doi.org/10.1364/OE.19.009783.
12. Shi, W.; Wang, M. An assessment of the black ocean pixel assumption for MODIS SWIR bands. *Remote Sens. Environ.* **2009**, 113(8), 1587–1597. https://doi.org/10.1364/OE.25.006015.
13. Pahlevan, N.; Smith, B.; Alikas, K.; Anstee, J.; Barbosa, C.; Binding, C.; Bresciani, M.; Cremella, B.; Giardino, C.; Gurlin, D.; Fernandez, V.; Jamet, C.; Kangro, K.; Lehmann, M.K.; Loisel, H.; Matsushita, B.; Ha, N.; Olmanson, L.; Potvin, G.; Simis, S.G.; VanderWoude, A.; Vantrepotte, V.; Ruiz-Verdu, A. Simultaneous retrieval of selected optical water quality indicators from Landsat-8, Sentinel-2, and Sentinel-3. *Remote Sens. Environ.* **2022**, 270, 112860. https://doi.org/10.1016/j.rse.2021.112860.
14. Franz, B.A.; Bailey, S.W.; Kuring, N; Werdell, P.J. Ocean color measurements with the Operational Land Imager on Landsat-8: implementation and evaluation in SeaDAS. *J. Appl. Rem. Sens.* **2015**, 9(1). https://doi.org/10.1117/1.JRS.9.096070.
15. Landsat 8 Data Users Handbook. Available online: https://www.usgs.gov/landsat-missions/landsat-8-data-users-handbook (accessed on 15 June 2022).
16. Landsat Collection 2. Available online: https://www.usgs.gov/landsat-missions/landsat-collection-2 (accessed on 17 June 2022).
17. Sinyuk, A.; Holben, B.N.; Eck, T.F.; Giles, D.M.; Slutsker, I.; Korkin, S.; Schafer, J.S.; Smirnov, A.; Sorokin, M.; Lyapustin, A. The AERONET Version 3 aerosol retrieval algorithm, associated uncertainties and comparisons to Version 2. *Atmos. Meas. Tech.* **2020**, 13, 3375–3411. https://doi.org/10.5194/amt-13-3375-2020.
18. Duntley, S. Q. Measurements of the distribution of water wave slopes. *J. Opt. Soc. Amer.* **1954**, 44 (7), 574–575. https://doi.org/10.1364/JOSA.44.0574_1.
19. Hwang, P.A.; Shemdin, O.H. The dependence of sea surface slope on atmospheric stability and swell conditions. *J. Geophys. Res.* **1988**, 93(C11), 13903–13912. https://doi.org/10.1029/JC093iC11p13903.
20. Fukushima, H.; Suzuki, K.; Li, L.; Suzuki, N.; Murakami, H. Improvement of the ADEOS-II/GLI sun-glint algorithm using concomitant microwave scatterometer-derived wind data. *Adv. Sp. Res.* **2009**. 43(6), 941–947. https://doi.org/10.1016/j.asr.2008.07.013.
21. Rascle, N.; Nouguier, F.; Chapron, B.; Mouche, A.; Ponte, A. Surface Roughness Changes by Finescale Current Gradients: Properties at Multiple Azimuth View Angles. *J. Phys. Oceanogr.* **2016**, 46, 3681–3694. https://doi.org/10.1175/JPO-D-15-0141.1.
22. Jackson, C. Internal Wave Detection Using the Moderate Resolution Imaging Spectroradiometer (MODIS). *J. Geophys. Res.* **2007**, 112, C11012:1-C11012:13. https://doi.org/10.1029/2007JC004220.
23. Askari, F. Multi-sensor remote sensing of eddy-induced upwelling in the southern coastal region of Sicily. *Int. J. Remote Sens.* **2001**, 22(15), 2899-2910. https://doi.org/10.1080/01431160119443.
24. Alpers, W.; Hühnerfuss, H. The damping of ocean waves by surface films: A new look at an old problem. *J. Geophys. Res.* **1989**, 94(C5), 6251–6265. https://doi.org/10.1029/JC094iC05p06251.
25. Hennings, I.; Matthews, J.; Metzner, M. Sun glitter radiance and radar cross-section modulations of the seabed. *J. Geophys. Res.* **1994**, 99(C8), 16303–16326, https://doi.org/10.1029/93JC02777.
26. Fresnel equations. Available online: https://en.wikipedia.org/wiki/Fresnel_equations (accessed on 20 June 2022).
27. Quan, X.; Fry, E. Empirical equation for the index of refraction of seawater. *Appl. Opt.* **1995**, 34, 3477-3480. https://doi.org/10.1364/AO.34.003477.
28. O'Reilly, J.E.; Maritorena, S.; Mitchell, B.G.; Siegel, D.A.; Carder, K.L.; Garver, S.A.; Kahru, M.; McClain, C.R. Ocean color chlorophyll algorithms for SeaWiFS. *J. Geophys. Res.* **1998**, 103, 24937-24953. https://doi.org/10.1029/98JC02160.
29. OceanColor WEB: Chlorophyll a. Available online: https://oceancolor.gsfc.nasa.gov/atbd/chlor_a/ (accessed on 20 June 2022).
30. Loisel, H.; Morel, A. Light scattering and chlorophyll concentration in case 1 waters: A reexamination. *Limnol. Oceanogr.* **1998**, 43(5), 847-858. https://doi.org/10.4319/lo.1998.43.5.0847.
31. Ocean Optics Web Book:. Dependence of R and R_{RS} on IOPs and Environmental Conditions. Available online: https://www.oceanopticsbook.info/view/inherent-and-apparent-optical-properties/reflectances (accessed on 20 June 2022).
32. Nechad, B.; Ruddick, K.G.; Park, Y. Calibration and validation of a generic multisensor algorithm for mapping of total suspended matter in turbid waters. *Remote Sens. Environ.* **2010**, 114 (4), 854-866. https://doi.org/10.1016/j.rse.2009.11.022.
33. Tomasi, C.; Vitale, V., Petkov, B., Lupi, A., Cacciari, A. Improved algorithm for calculations of Rayleigh-scattering optical depth in standard atmospheres. *Appl. Opt.* **2005**, 44(16), 3320–3341. https://doi.org/10.1364/AO.44.003320.

34. Dierssen, H.M. Hyperspectral Measurements, Parameterizations, and Atmospheric Correction of Whitecaps and Foam from Visible to Shortwave Infrared for Ocean Color Remote Sensing. *Front. Earth Sci.* **2019**, 7:14. https://doi.org/10.3389/feart.2019.00014.
35. Philpot, W. Estimating Atmospheric Transmission and Surface Reflectance from a Glint-Contaminated Spectral Image. *IEEE Trans. Geosci. Remote Sens.* **2007**, 45(2), 448-457. https://doi.org/10.1109/TGRS.2006.887161.
36. Rahman, H.; Dedieu, G. SMAC: a simplified method for the atmospheric correction of satellite measurements in the solar spectrum. *Int. J. Remote Sens.* **1994**, 15:1, 123-143. https://doi.org/10.1080/01431169408954055.
37. SMAC python code for atmospheric correction. Available online: https://github.com/olivierhagolle/SMAC/tree/master/COEFS (accessed on 15 June 2022).
38. Hersbach, H.; Bell, B.; Berrisford, P.; Biavati, G.; Horányi; A., Muñoz Sabater, J.; Nicolas, J.; Peubey, C.; Radu, R.; Rozum, I.; Schepers, D.; Simmons, A.; Soci, C.; Dee, D.; Thépaut, J-N. ERA5 hourly data on single levels from 1979 to present. Copernicus Climate Change Service (C3S) Climate Data Store (CDS) **2018**. Available online: https://doi.org/10.24381/cds.adbb2d47 (accessed on 15 June 2022).
39. Xu, H. Modification of normalised difference water index (NDWI) to enhance open water features in remotely sensed imagery. *Int. J. Remote Sens.* **2006**, 27:14, 3025-3033. https://doi.org/10.1080/01431160600589179.
40. Sang, B.; Schubert, J.; Kaiser, S.; Mogulsky, V.; Neumann, C.; Förster, K.P.; Hofer, S.; Stuffler, T.; Kaufmann, H.; Müller, A.; Eversberg, T.; Chlebek, C. The EnMAP hyperspectral imaging spectrometer: instrument concept, calibration, and technologies. Proc. SPIE 7086, Imaging Spectrometry XIII, 708605, San Diego, California, United States, 27 August 2008. https://doi.org/10.1117/12.794870.
41. MultiSpectral Instrument (MSI) Overview, Table 2: The temporal offset (in seconds) between selected bands. Available online: https://sentinels.copernicus.eu/web/sentinel/technical-guides/sentinel-2-msi/msi-instrument (accessed on 23 June 2022).
42. AERONET Aerosol Optical Depth Data Display Interface, Site: Brest_MF. Available online: https://aeronet.gsfc.nasa.gov/cgi-bin/data_display_aod_v3?site=Brest_MF (accessed on 29 June 2022).